Thermal dependence of large scale freckle defect formation

Kao, A.; Shevchenko, N.; Alexandrakis, M.; Krastins, I.; Eckert, S.; Pericleous, K.;

Originally published:

April 2019

Philosophical Transactions of the Royal Society A 377(2019)2143, 20180206

DOI: https://doi.org/10.1098/rsta.2018.0206

PHILOSOPHICAL TRANSACTIONS A

Phil. Trans. R. Soc. A.

doi:10.1098/not yet assigned

Thermal dependence of large scale freckle defect formation

A. Kao[1], N. Shevchenko[2], M. Alexandrakis[1], I. Krastins[1], S. Eckert[2], K. Pericleous[1]

[1]*Centre for Numerical Modelling and Process Analysis, University of Greenwich, Old Royal Naval College, Park Row, London, SE109LS, UK, ORCID-0000-0002-6430-2134*

[2]*Helmholtz-Zentrum Dresden-Rossendorf, Institute of Fluid Dynamics, Bautzner Landstrasse 400, 01328 Dresden, Germany*

Keywords: Freckle defect formation, Ga-In alloy, Convective transport

Summary

The fundamental mechanisms governing macroscopic freckle defect formation during directional solidification are studied experimentally in a Hele-Shaw cell for a low melting point Ga-25wt.%In alloy, and modelled numerically in 3D using a microscopic parallelised Cellular Automata lattice Boltzmann method. The size and distribution of freckles (long solute channels, or chimneys) is shown to be strongly dependent on the thermal profile of the casting, with flat, concave and convex isotherms being considered. For the flat isotherm case, no large-scale freckles form, while for concave or convex isotherms large freckles appear but in different locations. The freckle formation mechanism is as expected buoyancy-driven, but the chimney stability, its long-term endurance and its location, are shown to depend critically on the detailed convective transport through the inter-dendritic region. Flow is generated by curved isopleths of solute concentration. As solute density is different from that of the bulk fluid, gravity causes 'uphill' or 'downhill' lateral flow from the sample centre to the edges through the mush, feeding the freckle. An excellent agreement is obtained between the numerical model and real-time x-ray observations of a solidifying sample under strictly controlled temperature conditions.

Introduction

During alloy solidification partitioning of elements at the liquid-solid interface leads to segregation of solute. If the segregation region approaches meso-macro length scales and fully solidifies it leads to a heterogeneous

*Author for correspondence (a.kao@gre.ac.uk).

†Present address: Centre for Numerical Modelling and Process Analysis, University of Greenwich, Old Royal Naval College, Park Row, London, SE10 9LS, United Kingdom

material, where the discontinuity in composition and hence variation in material properties can have adverse effects on the performance of components. These solute enriched regions are known as freckle defects and are common in many industrial processes, for example Nickel-based superalloys, used to manufacture industrial gas turbine blades, can develop freckles [1-4], as well as steel ingots [5]. Freckles vary in size from O(100 μm) to O(1 cm), where O(…) designates the order of magnitude. Extensive work has been carried out demonstrating that there is a critical Rayleigh number (defined variously by Fellicelli *et al.* [6], Auburtin *et al.* [3] and Beckerman *et al.* [4]) which leads to the onset of freckles. Microscale numerical models [7-10] have captured the underlying mechanism that leads to small-scale freckle formation and successfully predicted this criterion and have revealed. However, due to the limitation on domain sizes in the simulations it is not possible to predict large-scale freckles, the size of which can be larger than the computational domains used. For larger scale freckles it has been necessary to use macroscale models [4,5,11,12], however this requires necessary assumptions about the microstructure, for example, porosity. Such assumptions are often empirical and while macroscale models have successfully predicted freckle formation and distribution, operating on this scale can obscure the fundamental mechanisms. With significant advances in parallel computing, resolving macroscale solidification from a microstructural perspective has become a reality using 100s of millions to billions of computational cells [13-15]. This is furthered by novel coupling of massively parallel methods, for example, in this work a cellular automata method [16,17] predicts solidification and operates on the larger end of the microscale. This is coupled to a lattice Boltzmann method that resolves the hydrodynamics with high efficiency [18-20].

This paper concerns the large-scale freckle formation that is often observed in the casting of Ni-based superalloy turbine blades. The partitioned solute in Ni-based superalloys is lighter than the bulk mixture, this leads to the formation of solute plumes, rising through the microstructure, emanating from the solid-liquid interface and dispersing back into the bulk. As the solute rises, it destabilises the thermal-solutal equilibrium preventing solidification, causing remelting and forming a channel. If the channel becomes stable, then as the cast continues to cool the channel will solidify as a freckle. Thermal conditions play a key role in the formation and distribution of freckles, for example, industry-focused large-scale experiments have shown [21] that there is a tendency for freckles to form on the boundary between the cast and the mould. Ni-based superalloys melt at a high temperature making experimental *in-situ* observations difficult. In terms of component density difference, the Gallium-Indium system shares many characteristics to Ni-based

superalloys but it is liquid at room temperature and much easier to handle. In this work, experiments are conducted on this analogue system. A parallel microstructure numerical study validated by these experiments is conducted investigating the large-scale mechanisms of freckle formation and how it is affected by macroscale thermal variations.

Experimental Method

The in-situ solidification experiments were carried out at Helmholtz-Zentrum Dresden-Rossendorf using an experimental setup which is described in detail in [22,23]. The experiments are performed in a Hele-Shaw cell made of quartz with a liquid metal volume of $29 \times 29 \times 0.15$ mm^3. The cell is filled with the low-melting-point hypereutectic Ga–25wt.%In alloy that is prepared from gallium and indium of 99.99 % purity. The solidification cells were produced in two geometric versions: a hexagonal cell and a rectangular one [24]. Two pairs of Peltier elements are mounted as a heater and as a cooler on the top edge and bottom edge of the solidification cell, respectively. The synchronized regulation of the power of both Peltier elements by means of a proportional-integral-derivative (PID) controller unit allowed the cooling rate and the temperature gradient to be adjusted during the process. In all experiments, the cooling rate was set at 0.01 K/s. The temperature difference ΔT between the heater and the cooler is measured using two miniature K-type (chromel–alumel) thermocouples, which make thermal contact to the outer surface of the cell near the edge of Peltier elements. The accuracy of the temperature control is ±0.3 K. The vertical temperature gradient was calculated from the temperature difference measured between these two thermocouples. The lateral temperature gradient was calculated from the complete temperature field which was measured by an infrared camera (Trotec IC 080 LV) equipped with an image sensor with a resolution of 384 x 288 pixels. Parameters of solidification experiments are shown in Table 1. The solidification setup was mounted on a three axis translation stage between a microfocus X-ray source (XS225D-OEM, Phoenix X-ray, Germany) and an X-ray detector (TH9438HX 9", Thales, France). In-situ and real-time observation of the solidification process was realized with an acquisition rate of 1 image per 1 second and with a spatial resolution of 5 – 10 microns.

The description of the image processing and analysis of the solidification front velocity can be found in [23,25]. The local composition of the solidifying alloy was determined from the relative brightness in the acquired X-ray images. The composition calibrations were performed by using reference measurements in cells filled with pure liquid Ga and with the Ga-25wt.%In alloy.

Numerical Method

The numerical model is a bespoke parallel Cellular Automata Lattice Boltzmann based Method (CALBM) designed specifically to handle convection driven solidification problems. The cellular automata method (CAM) part predicts the

evolution of the microstructure, while the lattice Boltzmann method (LBM) calculates the hydrodynamics. The two methods are linked by body forces and convective transport of heat and mass. To capture meso-macroscopic features from a microscopic perspective requires extensive parallelisation, which is achieved through domain decomposition using Message Passing Interface (MPI) for inter-process communications. This section provides a brief overview of the governing equations for each method, coupling of the methods and parallelisation. A more detailed description of the numerical method can be found here [26].

Cellular Automata Method

The CAM uses a continuous phase variable ϕ to represent solidification, where $\phi = 1$ is fully solid, $\phi = 0$ is fully liquid and intermediate values are solidifying. For alloy solidification the concentration of solute in the solid (C_s) and liquid (C_l) are governed by

$$C_s = kC_l, \tag{1}$$

where k is the partitioning coefficient of solute. The equivalent concentration, C_e, is defined as a linear relationship in ϕ between C_s and C_l given by

$$C_e = (1-\phi)C_l + \phi C_s. \tag{2}$$

At the interface, the solid fraction rate of change in time (t) is given by

$$C_l(1-k)\frac{\partial \phi}{\partial t} = -\nabla \cdot (D_e \nabla C_l) + [1-(1-k)\phi]\frac{\partial C_l}{\partial t}. \tag{3}$$

The equilibrium interface temperature, T^i, is calculated from the alloy phase diagram, which relates the melting temperature to the local concentration by

$$T^i - T_0 = m_l(C_l - C_0), \tag{4}$$

where m_l is the liquidus slope, C_0 is the initial concentration and T_0 is the liquidus temperature at C_0 [7]. Convective transport of solute is governed by

$$\frac{\partial C_e}{\partial t} + \mathbf{u} \cdot \nabla C_l = \nabla \cdot (D_e \nabla C_l), \tag{5}$$

where $\mathbf{u}$ is the flow velocity in the liquid, and $D_e = (1-\phi)D_l + \phi D_s$ is the equivalent diffusion coefficient, defined as a linear relationship in ϕ between D_s and D_l. Due to the low thermal Peclet number and high thermal diffusivity, the temperature is assumed to be known explicitly. Thus, during solidification, the temperature field simply becomes

$$\frac{\partial T}{\partial t} = -Q, \tag{6}$$

where Q (K/s) is the cooling rate. The relative buoyancy force acting on the liquid is expressed as

$$\mathbf{F} = \rho \mathbf{g}\big(\beta_T(T - T_0) + \beta_C(C - C_0)\big), \tag{7}$$

where ρ is the density, $\mathbf{g}$ is acceleration due to gravity, β_T and β_C are the thermal and solutal expansion coefficients and T_0 is a reference temperature.

Lattice Boltzmann Method

A three-dimensional D3Q19 lattice with 19 discrete velocities ($\mathbf{c}_i$) has been employed in this work to simulate hydrodynamics described by the Navier–Stokes equation (NSE),

$$\frac{\partial \mathbf{u}}{\partial t} + \mathbf{u} \cdot \nabla \mathbf{u} = -\frac{1}{\rho}\nabla p + \nu \nabla^2 \mathbf{u} + \mathbf{F}, \tag{8}$$

where ρ is the density, p is the pressure and ν is the kinematic viscosity. The NSE can be recovered from the lattice Boltzmann equation (LBE), which describes the evolution of a particle distribution function (PDF), f_i, in discrete space ($\mathbf{x}$) and time,

$$f_i(\mathbf{x} + \mathbf{c}_i \Delta t, t + \Delta t) - f_i(\mathbf{x}, t) = -\frac{1}{\tau}\left(f_i(\mathbf{x}, t) - f_i^{eq}(\mathbf{x}, t)\right) + F_i(\mathbf{x}, t)\Delta t, \tag{9}$$

through the Chapman-Enskog expansion, where Δt is the time step, f_i^{eq} is the equilibrium PDF and F_i is the force, linking the kinematic viscosity to the relaxation time, τ, as

$$\nu = \frac{c^2}{6}(2\tau - \Delta t), \tag{10}$$

where $c = \Delta x / \Delta t$ is the lattice speed with spatial step Δx. The TRT (two relaxation time) collision scheme is used in this work for stability purposes [27] modifying the LBE in equation (9) as

$$f_i(\mathbf{x} + \mathbf{c}_i \Delta t, t + \Delta t) = f_i(\mathbf{x}, t) + g_i^{+}(\mathbf{x}, t) + g_i^{-}(\mathbf{x}, t) + F_i(\mathbf{x}, t)\Delta t, \tag{11}$$

where

$$g_i^{\pm} = -\frac{1}{\tau^{\pm}}\left(f_i^{\pm} - f_i^{eq\pm}\right), \text{with } f_i^{\pm} = \frac{1}{2}(f_i \pm f_{\bar{\imath}}), \mathbf{c}_i = -\mathbf{c}_{\bar{\imath}}. \tag{12}$$

$\mathbf{c}_{\bar{\imath}}$ and $f_{\bar{\imath}}$ are pointed in the opposite direction of $\mathbf{c}_i$ and f_i and $\tau^{\pm}$ are the two relaxation times. The force F_i acting on the system is given by [28]

$$F_i = \left(1 - \frac{1}{2\tau}\right)\frac{3(\mathbf{c}_i - \mathbf{u}) \cdot \mathbf{a}}{c^2} f_i^{eq}, \tag{13}$$

where $\mathbf{a}$ is the acceleration. The equilibrium PDF f_i^{eq} is defined as

$$f_i^{eq} = \rho w_i \left(1 + 3\frac{\mathbf{c}_i \cdot \mathbf{u}}{c^2} + 9\frac{(\mathbf{c}_i \cdot \mathbf{u})^2}{2c^4} - 3\frac{\mathbf{u}^2}{2c^2}\right), \tag{14}$$

where w_i and $\mathbf{c}_i$ are the lattice weight coefficients and discrete velocities. Then, the density and fluid velocities can be calculated from the PDFs as

$$\rho = \sum_i f_i, \quad \rho \mathbf{u} = \sum_i f_i \mathbf{c}_i + \frac{\Delta t}{2}\mathbf{F}. \tag{15}$$

A 3D moment-based boundary method, which is an extension from 2D [29], is used for the velocity and pressure boundaries. The bounce-back scheme is used to describe the complex interior boundaries.

Parallelisation

The coupled CALBM algorithm is parallelised on Central Processing Units (CPUs) using the MPI-based libraries for inter-processor communication. The numerical domain is decomposed and distributed equally across all cores. The information exchange is handled through halo regions. The halo regions are populated with the physical boundary condition if they are domain boundaries, or with the neighbouring boundary information if they are inter-core boundaries. The halo regions are updated once every time step, and then are communicated across the neighbouring processes. The message-passing updates the halo regions in core pairs, sequentially for each direction.

Coupling

The fully coupled CALBM model utilises a separate spatial scale for each method. The ratio of the CAM scale to the LBM scale is restricted to powers of two. The two-way coupling between the CAM and LBM can also vary in strength by changing the ratio of their respective temporal scales. The spatial and temporal scales are generally linked through the Courant-Friedrichs-Lewy condition, as both methods are fully explicit, and their selection is problem-dependent. The spatial scales are chosen so that both microstructure and fluid flow features, such as secondary dendritic arm spacing (SDAS) and inter-dendritic flow, can be captured. The typical length scale of the inter-dendritic flow is much larger than the SDAS, thus a coarser grid to resolve the flow can be chosen to minimise the computational requirements. In this work, the ratios of both the spatial and temporal scales have been chosen as 4 and 50 respectively.

Problem Setup and Assumptions

The numerical model is a cuboid domain of size $32 \times 32 \times 0.16$ mm^3 populated with cubic cells of length 10 µm, giving a computational grid of $3200 \times 3200 \times 160 = 1.64$ billion cells, representing the macroscopic scale of the sample. All domain walls have zero velocity with no mass flux, except for the top wall, which is a zero-pressure boundary with bulk concentration conditions. Material properties used in the model represent Ga-25wt.%In and are given in Table 2. The lateral temperature variation is modelled by assuming that isotherms can be represented by an off-centred circle. When the centre of the circle is below the domain, the isotherms take a convex shape while if the centre of the circle is above the domain the isotherms become concave see also figures below). In all the cases presented, the thermal gradient is aligned with gravity, $G_z = 1.6$ K/mm and the cooling rate is taken as $Q = 0.0064$ K/s giving a characteristic solidification velocity of 4µm/s. Initially the lower boundary is nucleated with 20 evenly spaced seeds, then as the system cools these seeds begin to grow partitioning gallium into the liquid phase. The localised high concentration of gallium is lighter than the bulk fluid and generates a net force in the z-direction along the thermal gradient. Fluid flow is driven towards the bulk transporting with it the enriched gallium forming a plume of solute.

There is a disparity in the timescales between the numerical model and experiment. To ensure a good thermal contact the Peltier cooler overlaps with the sample in the experiment, such that *in situ* observation of this region is not possible. This overlapped region is up to 6mm and solidification would take 1500 s with 4µm/s growth. After nucleation, the local gallium rich liquid will introduce a constitutional undercooling, requiring further cooling, therefore it could take up to 2000 s before solidification is above the cooler. It also depends on the location of the field of view of experiments, where

to capture the final details this does not necessarily encompass the entire sample. Also, the time averaged velocity in the experiments was approximately 5 μm/s, slightly faster than the numerical model. Times quoted for experiments are based on the first observation of the solid front, while in the numerical results time is given from nucleation.

Results and Discussion

The first case considered is with flat isotherms, hence, the lateral thermal gradient in the x-direction, $G_x = 0$. With no variation in temperature normal to gravity there is no flow driven by thermal buoyancy as it is balanced by a hydrostatic pressure gradient. Natural convection is then driven by localised high concentrations of gallium escaping into the bulk. Figure 1 shows numerical (a-c) and experimental (d-f) results for the time evolution of the microstructure. Figure 1c also shows macroscopic contour lines of ϕ, which have been calculated by volume averaging over relatively large volumes of $1.6\text{mm} \times 160\mu\text{m} \times 1.6\text{mm}$. In both the numerical and experimental results no stable channel is formed. Small channels appear, but then after a short period the microstructure either grows into this region or overgrows the channel leaving small pockets of gallium rich liquid. These pockets are small scale freckles that have been captured theoretically, numerically and experimentally by other investigations and are generated when the Rayleigh number is above a critical value. The pockets appear throughout the entire microstructure and the mechanism for this behaviour can be attributed to the migration of plumes. As a plume forms, the high concentration of rising gallium remelts part of the microstructure and prevents solidification. However, to preserve continuity the high concentration flow leaving the interface is replaced by local inter-dendritic fluid, which in turn is fed by downward flow from the bulk. This low concentration downward flow promotes solidification, reducing the inter-dendritic porosity in local regions surrounding the plume. Eventually, the inter-dendritic regions can no longer feed the plume from the sides and by necessity, a counter flow from the bulk enters the channel encouraging solidification. The lighter liquid escapes and the plume destabilises; it either dissipates into the bulk or migrates to a new location on the interface. The contours of solid fraction ϕ in figure 1(c) show that in regions where these pockets have formed the values of ϕ are closer, indicating that solidification was encouraged in these regions. For example, on the lower right hand side of figure 1(c) the line of $\phi = 0.4$ extends high up into the mush, with pockets either side. At this location flow into this region fed the pockets until the value of ϕ increased and was unable to feed the channels. This unstable process continues throughout solidification and with no stable flow field forming at any point on the interface, no stable channel forms. The mechanism for this is highlighted in figure 1(g-i). Below the interface, the system drives to equilibrium between the liquid concentration and temperature. As the isotherms are flat, direct application of equation (4) also requires the isopleths of concentration to be flat. Therefore, the solute buoyancy force in the liquid regions of the mushy zone becomes constant in planes normal to gravity. This hydrostatically balanced system leads to very little residual flow from the mushy zone to the interface. Figure 1(g) highlights the flat isopleths through the liquidus concentration (the concentration if all cells were liquid). Figure 1(h) shows the z-component of velocity, the velocity of the plumes is O(1 mm/s), however the scale bar is purposefully scaled to slower velocities, for

comparison to subsequent cases but to also highlight that deep in the mushy zone there is effectively no flow. Figure 1(i) shows the relative pressure, Δp, which is calculated by removing the hydrostatic pressure. In this case small pressure variations only occur at the interface driving the small-scale circulations that are shown schematically on the figure, and highlighting that the mechanism for the formation of small pockets of gallium-enriched liquid is localised to plume and the interface. There is a direct analogy for this case to Rayleigh-Bernard flow, where the system quickly evolves into a chaotic state. With no time averaged spatial bias of convective transport of solute it is not possible to sustain a large scale channel.

Case 2 is with $G_x \approx 0.25$ K/mm and is representative of experimental results with a moderate thermal gradient. Figure 2 shows a comparison of numerical (a-c) and experimental (d-f) results of the microstructure time evolution, leading to the formation of a stable channel. Although thermal buoyancy now drives large-scale flow circulations, the results reveal that this is not the primary mechanism for the formation of the stable channel. Instead, the mechanism is driven by solute buoyancy forces. The temperature does play a key role, in that in the inter-dendritic regions the system drives to a thermo-solutal equilibrium and with the isotherms now convex, the concentration isopleths also take on a convex profile. With a cooler centre and higher concentration, the solute forces are stronger here than at the edge of the sample. This leads to a relative force in the inter-dendritic liquid that drives flow up the centre of the sample and down at the edges. This solute driven large-scale flow generates a net transport of high concentration gallium toward the centre through the inter-dendritic region causing re-melting of the microstructure and ultimately the formation of the channel. As the plume leaves the channel, it assists the channel formation by generating a suction force. This is highlighted in figure 2(g), which shows the liquid concentration and the entire microstructure is in thermo-solutal equilibrium except near the channel, where the re-melted liquid and high flow velocities prevent the system from reaching this equilibrium. Figure 2(h) shows the *x*-component of velocity with positive and negative values on the left and right respectively of the channel highlighting the large-scale flow necessary to form and sustain the channel. As the only driving force for flow is gravity directed in *z*, a pressure gradient forms in *x* to drive the inter-dendritic feeding flow. The relative pressure is shown in figure Figure 2(i) along with a schematic of the large-scale flow field.

Once a channel begins to form it is not immediately clear if it is due to the relative forced introduced by the convex isopleths of concentration or, as previously suggested [22], due to the suction force from escaping plumes. However, these results suggest that a bias is introduced from the convex isopleths of concentration. This argument is further supported by comparing the buoyancy force due to the high concentration gallium in the channel to the force generated by the convex isopleth of concentration. In the channel, from equation (7) the integral force of the solutal buoyancy can be described by $F_p = \rho g \beta_C (C_p - C_0) V_p$, where C_p is the concentration of the liquid in the channel, C_0 a reference concentration taken to be the thermal-solutal equilibrium concentration along the centre of the domain and $V_p = WDH_m$ is the volume of the channel, with dimension width, *W*, depth, *D* and height of the microstructure, H_m. The integral force in the inter-dendritic fluid can be expressed as $F_m = \rho g \beta_C (C_m - C_0) V_m (1 - \phi)$, where $V_m(1 - \phi)$ is the volume of the

inter-dendritic fluid and $V_m = (L - W)DH_m$, where L is the length of the sample. A schematic of the relevant lengths is given in figure 3. C_m is the integral concentration in the inter-dendritic region. From equation (4) and with $C_m = C_l$, C_m can be obtained by integration with respect to x

$$2\int_0^{\frac{L}{2}-\frac{W}{2}} G_x dx = \int_0^{\frac{L}{2}-\frac{W}{2}} m_l \frac{\partial(C_m - C_0)}{\partial x} dx \tag{16}$$

giving

$$C_m - C_0 = \frac{G_x}{m_l}(L - W). \tag{17}$$

From both the experimental and numerical results the width of a channel is typically O(1 mm). For the experimental conditions and material properties, this gives a concentration difference between the edge and the centre of the sample $C_m - C_0 \approx 3$wt. % The relative strength of these two forces becomes

$$\frac{F_p}{F_m} = \frac{(C_p - C_0)W}{\frac{G_x}{m_l}(L - W)^2(1 - \phi)}. \tag{18}$$

Using the numerical results the average value of $\phi = 0.4$ was calculated in the microstructure.

In the channel C_p is assumed constant; it is the thermo-solutal equilibrium that changes. At the base of the channel it can be assumed that $C_0 = C_p$ then varying linearly to the bulk concentration at the top of the channel. As it is the term $C_p - C_0$ that determines the force, it is strongest at the top of the interface. In both experiments and the numerical models the initiation of the channel begins with Gallium concentrations around 80 wt.% Substituting this into equation (18) gives a relative force $\frac{F_p}{F_m} = 0.1$ indicating that although both forces are acting in the same direction, it is the force in the inter-dendritic fluid that is more likely to initiate the formation of a channel. Even in the unrealistic case where channel is 100% Gallium the relative force is still $\frac{F_p}{F_m} = 0.5$. Although this solution suggests the initiation is due to the forces in the inter-dendritic liquid it does not consider the suction force that would be present for a fully formed channel. However, this solution can be further extended to investigate the relative effect of the suction force a sustained plume would have on a fully formed channel. To compare the suction force of the plume to the relative forced introduced by the convex isopleths of concentration, assume the plume has a height H_p and the microstructure has a height H_m. The ratio of forces then becomes

$$\frac{F_p}{F_m} = \frac{(C_p - C_0)WH_p}{\frac{G_x}{m_l}(L - W)^2(1 - f)H_m}. \tag{19}$$

By setting $\frac{F_p}{F_m} = 1$, the ratio of the plume height to the microstructure height for these experimental conditions becomes $H_p/H_m = 2.1$ for a Ga concentration of 90 wt.% and increasing for a Ga concentration of 80 wt.% to $H_p/H_m = 6.4$. Given that the earliest height where stable channels are observed is around 10 mm, the plume would need to be on the scale or larger than the entire sample. This also implies that for a plume with a velocity of O(1 mm/s) it will take 21 s to

develop for 90 wt.% Gallium. However, as the plume dissipates it will also decelerate so this time scale will be longer. Dissipation of the plume can be estimated from equation (5) with $C_e = C_l$ and $D_e = D_l$ by approximating the operators $\frac{\partial C_e}{\partial t} \approx \frac{\Delta C_l}{\Delta t}, \nabla \cdot (D_e \nabla C_l) \approx \frac{D_l \Delta C_l}{\Delta x_D^2}$ and $\mathbf{u} \cdot \nabla C_l \approx \frac{u_r \Delta C_l}{\Delta x_D}$ to give

$$\frac{\Delta C_l}{\Delta t_D} = \frac{D_l \Delta C_l}{\Delta x_D^2} - \frac{u_r \Delta C_l}{\Delta x_D}, \tag{20}$$

where ΔC_l, which cancels, represents change in concentration over the diffusion time scale Δt_D and diffusion length scale Δx_D. The velocity u_r accounts for radial flow circulations near the tip of the plume. With $u_r = 0$ in 21 s the diffusion length scale is 207 µm. However, even with a moderate radial flow of 100 µm/s the transported length scale becomes 3.2 mm, much larger than the plume itself. It is unlikely that such a large plume would be sustained and consequently unable to supply a strong enough suction force to become the dominant mechanism. In the case of large-scale casts, where at some distance below the interface the eutectic forms the length H_m is known and for these experimental parameters would be O(20-30 mm). Therefore, the plume would need to be at least O(40-60 mm) high to provide an equal suction force to inter-dendritic solute buoyancy force.

In the initial stages of solidification, the channel is not stable, an unstable behaviour observed both in the experiments and in the numerical results. Channels form, but cannot be sustained by the inter-dendritic flow, this can be explained by looking at mass balance. Consider a channel of width W that is being fed by a microstructure with height H. Balancing the mass flux at the exit of the channel to mass entering the channel from the microstructure gives $u_p W = 2u_m H(1 - \phi)$, where u_p is the velocity of the channel and u_m the inter-dendritic fluid velocity. In this work, stable channels typically have $u_p = 1$ mm/s with $W = 1$ mm. From the numerical results u_m = O(50-100 µm/s), H can be calculated to be 8-16 mm for $\phi = 0.4$ and 6-13 mm for $\phi = 0.2$. Two estimates of ϕ are given as they encompass the predictions of the numerical model as ϕ increases over time while slow solidification occurs whilst feeding the formation. This simple calculation is in good agreement with both the numerical and experimental observations. During this unstable formation regime, oscillations between solidification and re-melting occur with the channel size ultimately increasing. This is highlighted both in the numerical and experimental results in figure 4(a,c) which shows that when the inter-dendritic liquid cannot feed the channel, downflow from the bulk is introduced, leading to rapid to solidification and closing of the channel as shown in figure 4(b,d). This process is similar to Case 1, but here the channels will reopen again due to the inherent bias introduced by the convex isotherms. Due to the influx of low concentration liquid, the re-solidification process occurs over a short time scale of O(10-100 s). When the channel closes off, gallium plumes will seek alternative passages into the bulk. This leads to a competition between channels to release gallium, and in some instances this can lead to ejected gallium oscillating between two channels. This behaviour is analogous to a fluidic oscillator and figure 5 shows this behaviour captured in both the numerical and experimental results. In the numerical results figure 5(a-b) shows that initially, the gallium is being ejected from the left channel and that a short time later (100 s) the plume is coming from the right-side channel. Similarly, in the experimental results figure 5(e-f) shows the same behaviour but with the channels reversed. This fluidic oscillator behaviour is a function of local porosity and inter-dendritic flow.

Gallium flowing out of one of the channels is fed by local fluid from the inter-dendritic region, which in turn is fed from the bulk. The low concentration bulk flow encourages growth reducing the porosity and at some point, it can no longer feed the channel, the plume pinches off and the gallium flows through the other channel. As the porosity decreases, the pressure in this region increases. Consequently, the oscillation between channels comes down to an oscillation in pressure, much like the behaviour in the feedback tubes of a fluidic oscillator. The corresponding pressure drops are highlighted in the numerical results in figure 5(c-d) for each channel. The process can repeat itself until the two channels merge, then as the microstructure continues to grow the volume of inter-dendritic fluid increases and inter-dendritic liquid can sustain the channel for longer periods of time until eventually the channel becomes stable.

The final case is where $G_x < 0$ is giving a cooler temperature at the edges of the sample and a hotter centre. This case is more typical of industrial casting applications where heat is lost through the mould of the cast. Generating this kind of thermal field was not possible with the current experimental set up and so Figure 6 shows numerical results only for the evolution of the microstructure. In contrast to Case 2, Figure 6(a-c) shows that the interface takes on a 'U' shape with stable channels forming on both edges of the sample. The mechanism for this formation essentially follows the same argument as Case 2, but in this case the thermo-solutal equilibrium generates a relative force upwards at the sample edge and downwards at the centre. This creates a bias where in the latter stages of solidification the solute plumes form at the edges. However, a key difference between these two cases is that there is also the interaction of the solute plume with the sample wall. Once the solute channel has fully melted through the solid, it attaches to the wall through the Coandă effect. Although this effect also occurs in Case 2 through the interaction of merging channels, the static wall allows the channel to fully attach and in an ideal perfectly smooth wall the channel remains fully attached all the way into the bulk. Figure 6(d) shows the liquid Ga concentration indicating that the only region where temperature and solute are not in equilibrium is in the channels. This figure also highlights how this temperature field introduces a bias for the channels to form at the edge, which is consistent with industry related experiments that show a general tendency for freckles to form between on the boundary of the cast and the mould [21]. Figure 6(e) shows the *x*-component of velocity with flow in the opposite direction to Case 2 with negative and positive values on the left and right respectively. This lateral flow through the inter-dendritic region is driven by a pressure gradient in *x*. The relative pressure is shown in figure Figure 6(f) along with a schematic of the large-scale flow field.

Conclusions and Future Work

The application of a parallel CALBM microscale numerical model has revealed fundamental mechanisms for the formation and stability of large-scale freckle defects. An excellent match between the numerical model and experiments conducted on thin sample Ga-25wt.%In alloy was achieved. Three cases representing flat, concave and convex isotherms demonstrated that the distribution and size of freckles is strongly dependent

on the transverse thermal profile. With a flat isotherm, no large-scale channels were observed, however the mechanisms for small- scale freckles were captured. For a convex isotherm a large stable channel formed in the centre of the sample and for a concave isotherm two stable channels attached to the sample wall. A comparison of forces revealed that the force due to curved isopleths of concentration is the dominant mechanism for large-scale channel formation and stability compared to the suction force from escaping plumes.

Strong lateral flow through the inter-dendritic region driven by a lateral pressure gradient was shown to be the feeding mechanism for stable channels. This pressure gradient is a direct consequence of the curved isopleths of concentration. To preserve continuity the lateral flow required large scale circulations and in regions where flow was incident from the bulk into the mushy zone solidification was encouraged resulting in an increase in solid fraction.

With an improved understanding of the mechanism, there are avenues of future study, primarily developing methods that can remove the freckle formation bias introduced by the thermal field. One possibility is the introduction of external forces, for example Lorentz force from external magnetic fields. This could be used to introduce additional fluid flow, or to counteract the lateral pressure gradient that feeds channels. Although, the parallel modelling technique deployed in this work is on the macro scale, there is still much development required in computing resources to realise large component scale simulations. However, by resolving the microstructure at macroscopic scales allowed for integrated values of the solid fraction to be predicted. These may be useful for improving, macroscale porosity modelling assumptions that are still necessary for component scale modelling.

Additional Information

Data Accessibility

The datasets supporting this article have been uploaded to the University of Greenwich's repository, available from gala.gre.ac.uk.

Authors' Contributions

AK carried out the numerical simulations and analysis, developed the parallel framework and coupling of the methods, and drafted the manuscript. NS and SE conducted the experiments and experimental analysis. IK developed the lattice Boltzmann method and drafted the manuscript. MA developed the cellular automata method. KP drafted the manuscript. All authors read and approved the manuscript.

Competing Interests

The authors declare that they have no competing interests.

Funding Statement
M. Alexandrakis and I. Krastins PhD studies were funded under the University of Greenwich Vice Chancellor postgraduate grant scheme.

References

1. 1. Reed RC, Tao T, Warnken N. 2009. Alloys-by-design: application to nickel-based single crystal superalloys. *Acta Mater.* **57**(19), 5898-913. (https://doi.org/10.1016/j.actamat.2009.08.018)
2. Madison JD. Investigation of Solidification Defect Formation by Three-Dimensional Reconstruction of Dendritic Structures. University of Michigan; 2010. (http://hdl.handle.net/2027.42/76001)
3. Auburtin P, Wang T, Cockcroft SL, Mitchell A. 2000. Freckle formation and freckle criterion in superalloy castings. *Metall. Mater. Trans.* B **31**(4), 801-11. (https://doi.org/10.1007/s11663-000-0117-9)
4. Beckermann C, Gu JP, Boettinger WJ. 2000. Development of a freckle predictor via Rayleigh number method for single-crystal nickel-base superalloy castings. *Metall. Mater. Trans. A* **31**(10), 2545-57. (https://doi.org/10.1007/s11661-000-0199-7)
5. Pickering EJ. 2013. Macrosegregation in steel ingots: the applicability of modelling and characterisation techniques. *ISIJ Int.* **53**(6), 935-49. (https://doi.org/10.2355/isijinternational.53.935)
6. Felicelli SD, Heinrich JC, Poirier DR. 1998. Finite element analysis of directional solidification of multicomponent alloys. *Int. J. Numer. Meth. Fluids* **27**(1-4), 207-27. (https://doi.org/10.1002/(SICI)1097-0363(199801)27:1/4%3C207::AID-FLD660%3E3.0.CO;2-X)
7. Wang W, Lee PD, Mclean M. 2003. A model of solidification microstructures in nickel-based superalloys: predicting primary dendrite spacing selection. *Acta Mater.* **51**(10), 2971-87. (https://doi.org/10.1016/S1359-6454(03)00110-1)
8. Yuan L, Lee PD. 2010. Dendritic solidification under natural and forced convection in binary alloys: 2D versus 3D simulation. *Model Simul. Mater. Sc.* **18**(5), 055008. (https://doi.org/10.1088/0965-0393/18/5/055008)
9. Yuan L, Lee PD. 2012. A new mechanism for freckle initiation based on microstructural level simulation. *Acta Mater.* **60**(12), 4917-26. (https://doi.org/10.1016/j.actamat.2012.04.043)
10. Karagadde S, Yuan L, Shevchenko N, Eckert S, Lee PD. 2014. 3-D microstructural model of freckle formation validated using in situ experiments. *Acta Mater.* **79**, 168-80. (https://doi.org/10.1016/j.actamat.2014.07.002)
11. Frueh C, Poirier DR, Felicelli SD. 2002. Predicting freckle-defects in directionally solidified Pb–Sn alloys. *Mat. Sci. Eng. A* **328**(1–2), 245-255. (https://doi.org/10.1016/S0921-5093(01)01700-2)
12. Saad A, Gandin CA, Bellet M, Shevchenko N, Eckert S. 2015. Simulation of Channel Segregation During Directional Solidification of In—75 wt pct Ga: Qualitative Comparison with InSitu Observations. *Metall. Mat. Trans. A* **46**, 4886. (https://doi.org/10.1007/s11661-015-2963-8)
13. Shimokawabe T, Aoki T, Takaki T, Endo T, Yamanaka A, Maruyama N, Nukada A, Matsuoka S. 2011. Peta-scale phase-field simulation for dendritic solidification on the TSUBAME 2.0 supercomputer. *Proceedings of 2011 International Conference for High Performance Computing, Networking, Storage and Analysis*, 1-11. (http://doi.org/10.1145/2063384.2063388)
14. Takaki T, Shimokawabe T, Ohno M, Yamanaka A, Aoki T. 2013. Unexpected selection of growing dendrites by very-large-scale phase-field simulation. *J. Cry. Growth.* **382**, 21-25. (https://doi.org/10.1016/j.jcrysgro.2013.07.028)
15. Eshraghi M, Jelinek B, Felicelli SD. 2015. Large-scale three-dimensional simulation of dendritic solidification using lattice Boltzmann method. *JOM* **67**(8), 1786-92. (https://doi.org/10.1007/s11837-015-1446-0)
16. Lee PD, Atwood RC, Dashwood RJ, Nagaumi H. 2002. Modeling of porosity formation in direct chill cast aluminum–magnesium alloys. *Mater. Sci. Eng. A* **328**(1-2), 213-22. (https://doi.org/10.1016/S0921-5093(01)01687-2)
17. Dong HB, Lee PD. 2005. Simulation of the columnar-to-equiaxed transition in directionally solidified Al–Cu alloys. *Acta Mater.* **53**(3), 659-668. (https://doi.org/10.1016/j.actamat.2004.10.019)
18. Yin H, Felicelli SD, Wang L. 2011. Simulation of a dendritic microstructure with the lattice Boltzmann and cellular automaton methods. *Acta Mater.* **59**(8), 3124-36. (https://doi.org/10.1016/j.actamat.2011.01.052)

19. Eshraghi M, Felicelli SD, Jelinek B. 2012. Three dimensional simulation of solutal dendrite growth using lattice Boltzmann and cellular automaton methods. *J. Cry. Growth* **354**(1), 129-34. (https://doi.org/10.1016/j.jcrysgro.2012.06.002)
20. Eshraghi M, Hashemi M, Jelinek B, Felicelli SD. 2017. Three-dimensional lattice Boltzmann modeling of dendritic solidification under forced and natural convection. *Metals* **7**(11), 474. (https://doi.org/10.3390/met7110474)
21. Hong J, Ma D, Wang J, Wang F, Sun B, Dong, Li F, A, Bührig-Polaczek A. 2016. Freckle defect formation near the casting interfaces of directionally solidified superalloys. *Materials* **9**(11), 929. (http://dx.doi.org/10.3390/ma9110929)
22. Shevchenko N, Boden S, Gerbeth G, Eckert S. 2013. Chimney formation in solidifying Ga-25wt pct In alloys under the influence of thermosolutal melt convection. *Metall. Mater. Trans. A* **44**(8), 3797-808. (https://doi.org/10.1007/s11661-013-1711-1)
23. Shevchenko N, Roshchupkina O, Sokolova O, Eckert S. 2015. The effect of natural and forced melt convection on dendritic solidification in Ga–In alloys. *J. Cry. Growth* **417**, 1-8. (https://doi.org/10.1016/j.jcrysgro.2014.11.043)
24. Shevchenko N, Eckert S, Boden S, Gerbeth G. 2012. In situ X-ray monitoring of convection effects on segregation freckle formation. *IOP Conference Series: Mat. Sci. Eng.* **33**(1), 012035. (https://doi.org/10.1088/1757-899X/33/1/012035)
25. Boden S, Eckert S, Willers B, Gerbeth G. 2008. X-ray radioscopic visualization of the solutal convection during solidification of a Ga-30 wt pct in alloy. *Metall. Mater. Trans. A* **39**(3), 613-23. (https://doi.org/10.1007/s11661-007-9462-5)
26. Kao A, Krastins I, Alexandrakis M, Shevchenko N, Eckert S, Pericleous K. 2018. A parallel cellular automata lattice Boltzmann method for convection-driven solidification. *JOM. Nov 12:1-1*. (https://doi.org/10.1007/s11837-018-3195-3)
27. Ginzbourg I, Adler P. 1994. Boundary flow condition analysis for the three-dimensional lattice Boltzmann model. *J. Phys. II* **4**,191–214.
28. He X, Shan X, Doolen GD. 1998. Discrete Boltzmann equation model for nonideal gases. *Phys. Rev. E* **57**(1), R13. (https://doi.org/10.1103/PhysRevE.57.R13)
29. Bennett S, Asinari P, Dellar PJ. 2012. A lattice Boltzmann model for diffusion of binary gas mixtures that includes diffusion slip. *Int. J. Numer. Meth. Fluids* **69**(1), 171-89. (https://doi.org/10.1002/fld.2549t)

Tables

Table 1. Experimental parameters of solidification experiments.

	Temperature gradient G_z, K/mm	Lateral gradient G_x, K/mm	Solidification cell
Experiment 1	1.6	~ 0	rectangular
Experiment 2	1.5 – 1.9	0.3 - 0.5	hexagonal
Experiment 3	1.4	~ 0	rectangular

Table 2. Material properties used in simulations.

Property	Variable	Value	Unit
Density Ga	ρ_{Ga}	6095	$\mathrm{kg\,m^{-3}}$
Density In	ρ_{In}	7020	$\mathrm{kg\,m^{-3}}$
Kinematic viscosity	ν	3.28 X 10^{-7}	$\mathrm{m^2 s^{-1}}$
Partitioning coefficient	k	0.5	-
Solute diffusivity	D_l	2 X 10^{-9}	$\mathrm{m^2 s^{-1}}$
Liquidus slope	m_l	2.9	$\mathrm{K\,wt.\,\%^{-1}}$
Solute expansion coefficient	β_C	1.66 X 10^{-3}	$\mathrm{wt.\,\%^{-1}}$
Thermal expansion coefficient	β_T	1.18 X 10^{-4}	$\mathrm{K^{-1}}$

Figure and table captions

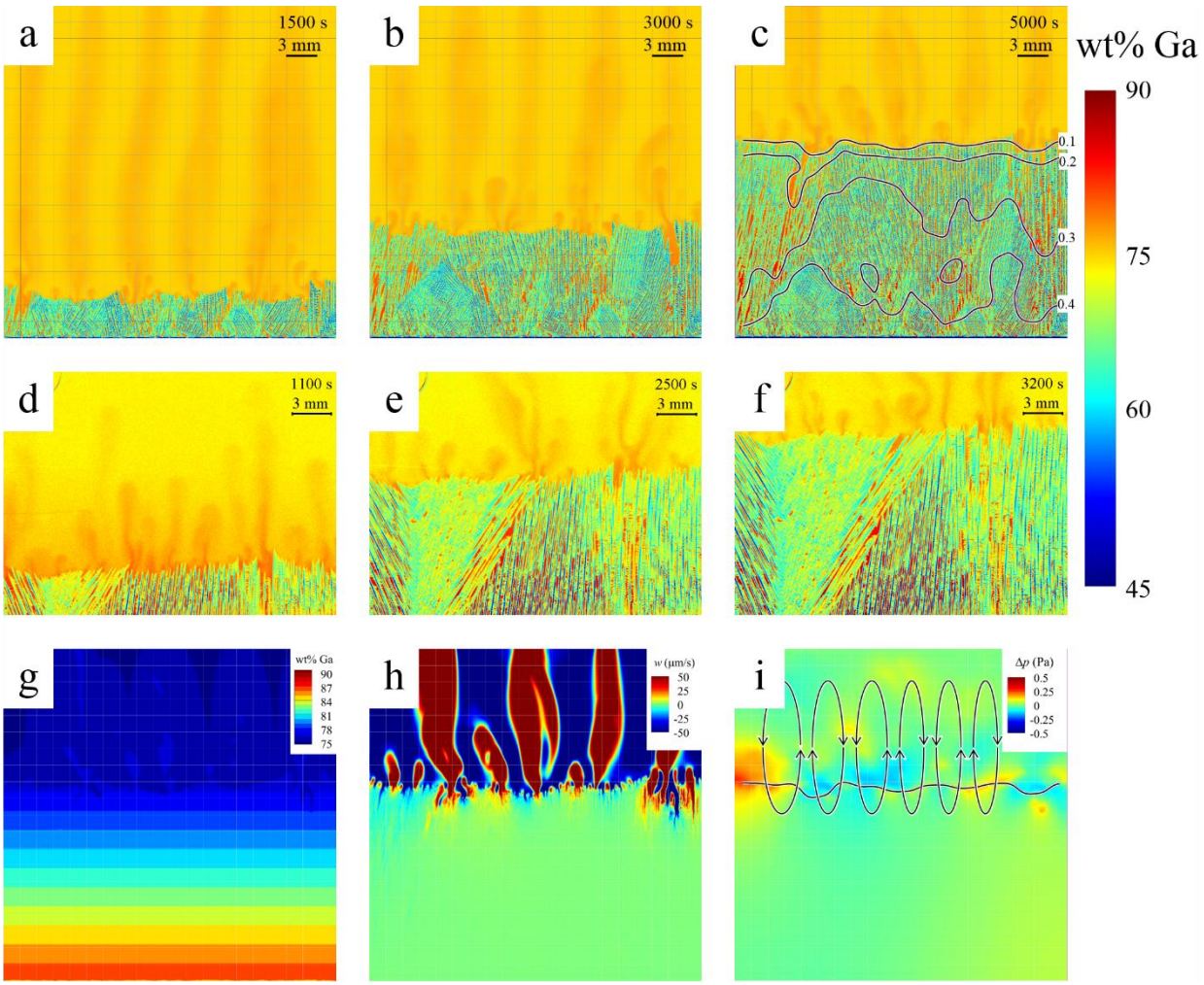

Figure 1. Case 1 with $G_x = 0$. a-c) Numerical results of evolution of microstructure at times a) 1500 s, b) 3000 s, c) 5000 s with contours of ϕ. d-f) Experimental results of microstructure evolution at times d) 1100 s, e) 2500 s, f) 3200 s. Numerical results at 5000 s of g) liquidus concentration, h) z-component of flow, i) relative pressure.

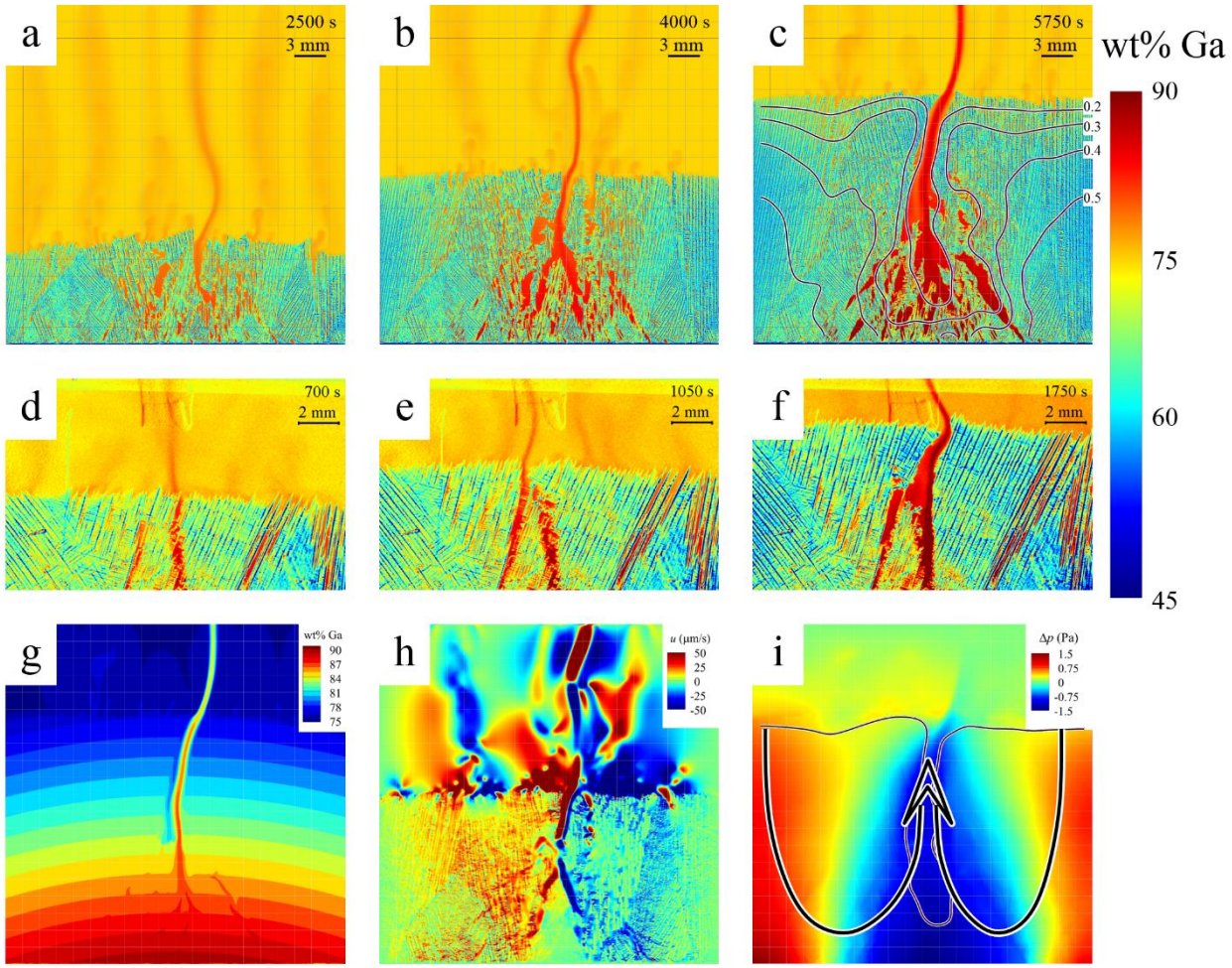

Figure 2. Case 2 with $G_x \approx 0.25$ K/mm. a-c) Numerical results of evolution of microstructure at times a) 2500 s, b) 4000 s, c) 5750 s with contours of ϕ. d-f) Experimental results of microstructure evolution at times d) 700 s, e) 1050 s, f) 1750 s. Numerical results at 4000 s of g) liquidus concentration, h) x-component of flow, i) relative pressure at 5750 s with schematic of large scale flow.

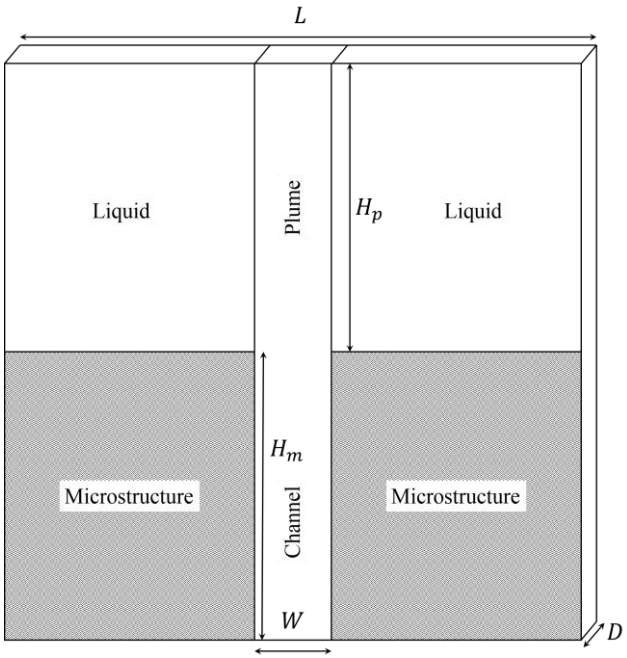

Figure 3. Schematic of lengths used to compare forces between the relative force from the isopleths of concentration with the force from the channel and from the suction force of the plume.

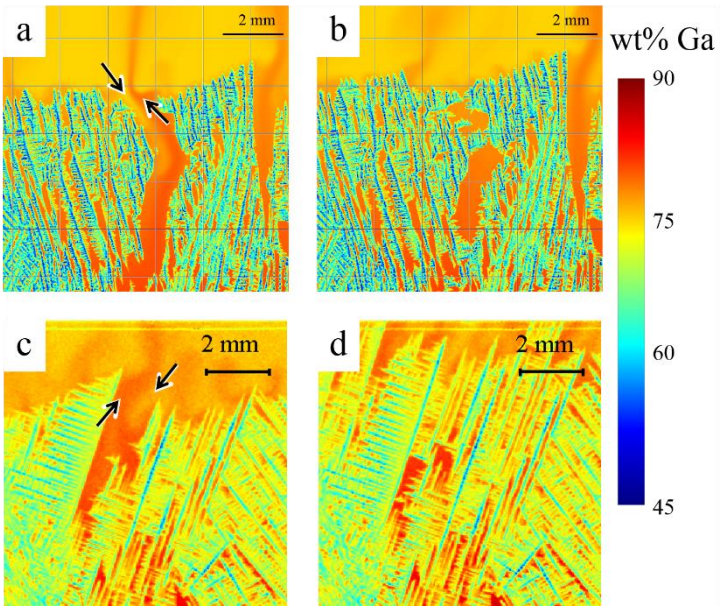

Figure 4. Channel closing mechanism. a,c) Numerical and experimental results respectively of the open channel with arrows highlighting the inflow of bulk concentration and the outflow of Gallium enriched liquid.

b,d) Numerical and experimental results respectively showing the closed channel.

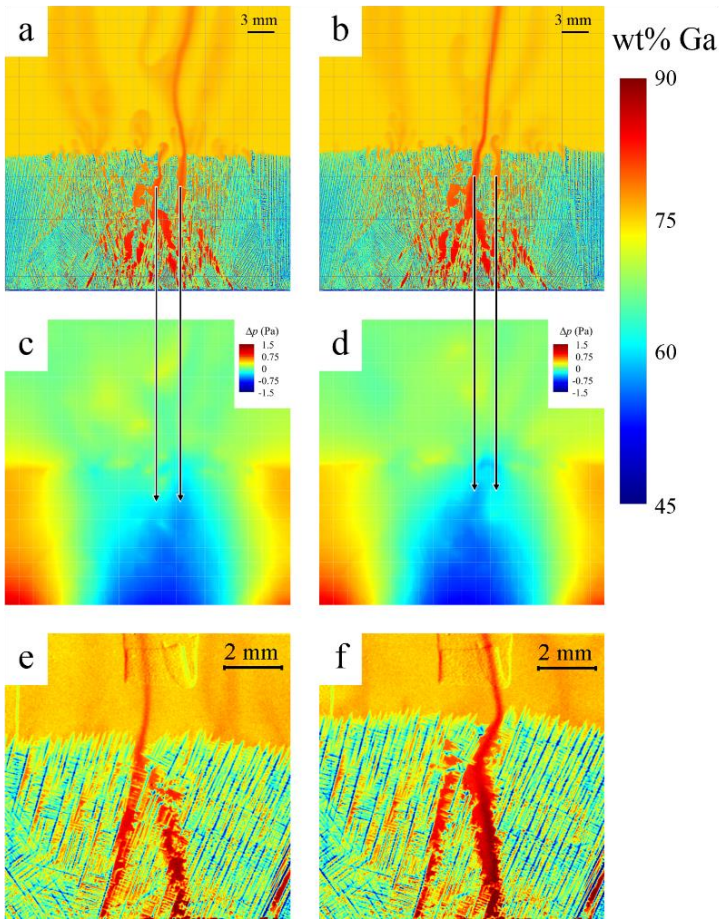

Figure 5. Fluidic oscillator between two competing chanels. a,b) Numerical results showing Gallium expelled from the right channel and then later by the left. c,d) relative pressure with location of channels indicated by arrows. e,f) Experimental results showing the same effect, but with channel oscillation reveresed.

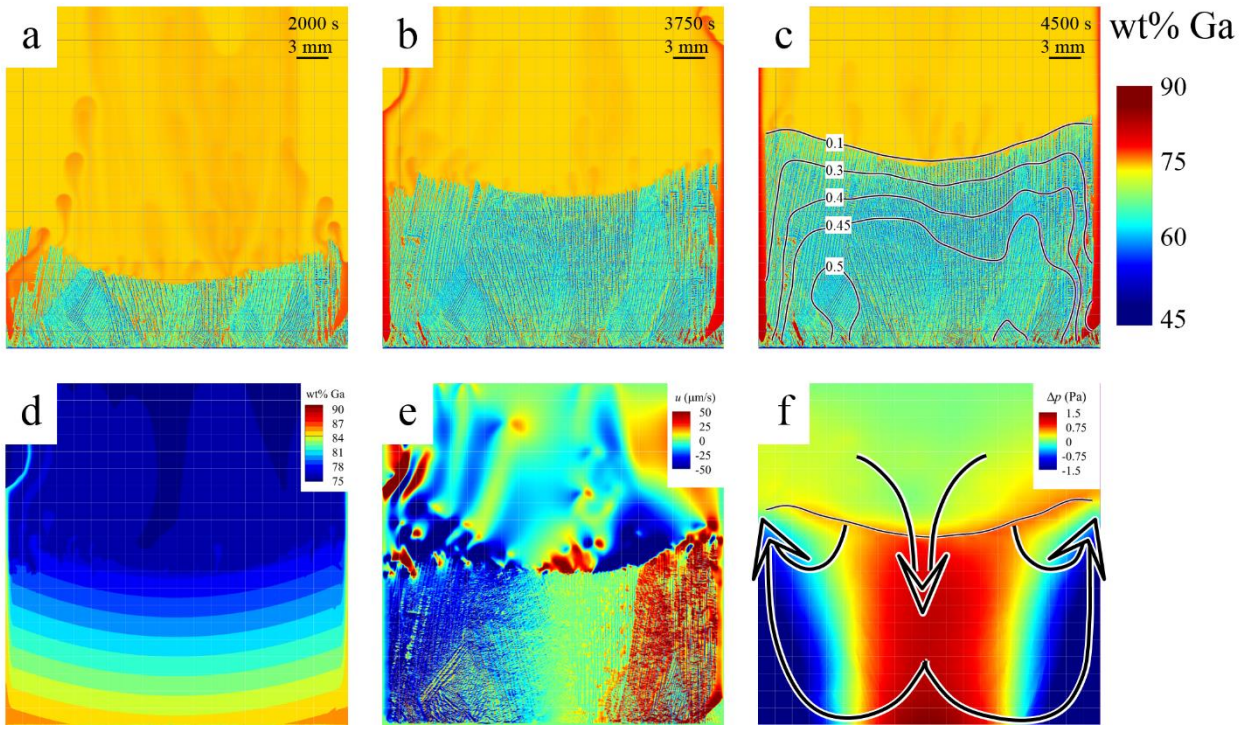

Figure 6. Case 3 with $G_x \approx -0.25$ K/mm. a-c) Numerical results of evolution of microstructure at times a) 2000 s, b) 3750 s, c) 4500 s with contours of ϕ. d-f) Numerical results at 3750 s of d) Ga liquid concentration, e) x-component of flow, f) relative presure at 4500 s with schematic of large scale flow.